

Compressively characterizing high-dimensional entangled states with complementary, random filtering

Gregory A. Howland,^{1,2,*} Samuel H. Knarr,^{1,†} James Schneeloch,^{1,2} Daniel J. Lum,¹ and John C. Howell¹

¹*Department of Physics and Astronomy, University of Rochester
500 Wilson Blvd, Rochester, NY 14627, USA*

²*Air Force Research Laboratory
525 Brooks Rd, Rome, NY 13441*

The resources needed to conventionally characterize a quantum system are overwhelmingly large for high-dimensional systems. This obstacle may be overcome by abandoning traditional cornerstones of quantum measurement, such as general quantum states, strong projective measurement, and assumption-free characterization. Following this reasoning, we demonstrate an efficient technique for characterizing high-dimensional, spatial entanglement with one set of measurements. We recover sharp distributions with local, random filtering of the same ensemble in momentum followed by position—something the uncertainty principle forbids for projective measurements. Exploiting the expectation that entangled signals are highly correlated, we use fewer than 5,000 measurements to characterize a 65,536-dimensional state. Finally, we use entropic inequalities to witness entanglement without a density matrix. Our method represents the sea change unfolding in quantum measurement where methods influenced by the information theory and signal-processing communities replace unscalable, brute-force techniques—a progression previously followed by classical sensing.

Practicing experimentalists most commonly perform quantum measurement in the context of state and parameter estimation [1]. While great historical emphasis has been placed on using measurement to probe the validity of quantum mechanics itself—where measurements must not only agree with quantum predictions but also rule out any competing explanations [2]—state estimation accepts quantum theory *a priori*. Here, measurements on identically prepared copies of a system are used to generate a model from which *testable* predictions can be made about future measurement statistics [3]. This point of view lifts the burden of validation, leading to simpler experiments and technologies.

Even so, quantum state estimation remains a persistent obstacle for scaling quantum technologies. The familiar approach of quantum tomography (QT) scales at least quadratically poorly with added dimensions and exponentially poorly with added particles. QT in an N -dimensional Hilbert space requires of order N^2 measurements [4]—when N is a prime power, N projections are taken in each of $N + 1$ mutually unbiased bases [5]. For example, tomography of a single spin qubit ($N = 2$) requires dividing the ensemble three ways, where expectation values of the \hat{X} , \hat{Y} and \hat{Z} spin components are separately measured. For most non-trivial quantum systems, traditional, brute-force QT is unmanageable in the lab. In particular, continuous-variable degrees-of-freedom, such as transverse-position and transverse-momentum or energy and time, where $N \rightarrow \infty$, cannot be realistically characterized via QT [6].

Efforts to overcome the limitations of QT fall into three major categories. First, often only a subset of a system’s behavior is of interest; e.g., if one only needs to predict a qubit’s spin

along one axis, information about the other two is irrelevant. The general tomographic density matrix can here be discarded in favor of simpler models [7]. A practical example is quantum key distribution (QKD), where only two (instead of order N) bases, such as energy and time, need be characterized [8]. Many entanglement witnesses only require a small subset of possible measurements to confirm entanglement [9, 10].

Second, one can leverage prior knowledge about a system. In standard tomography, maximum likelihood estimation is used to find a valid density matrix consistent with measurement data [11, 12]—a simple assumption that quantum mechanics holds. Or, given a model of the physical system, one can begin with a prior distribution which is updated or parameterized in response to measurements, as in Bayesian inference [13, 14].

One powerful presupposition is that a signal is structured, or *compressible*. For classical signals, this surprisingly broad assumption spawned the field of compressed sensing (CS) to tremendous multidisciplinary impact [15, 16] with a strong presence in imaging [17–20]. In compressed sensing, signals are compressed during measurement so they can be sampled below the Nyquist limit [21]. Several recent efforts apply CS to quantum measurement to dramatic effect [22–26]—in some cases reducing measurement times from years to hours [27]. For tomography, all protocols exploiting positivity are a form of compressed sensing [28].

Finally, one can choose measurements well suited to the model and prior knowledge. There is a compelling movement beyond traditional, projective measurements that localize quantum particles. Notably, there is weak measurement, where a system and measurement device are very weakly coupled, leaving the system nearly undisturbed [29]. With weak measurement, researchers have directly measured the quantum wavefunction [30], observed average trajectories of particles in the double-slit experiment [31], and performed tests of local realism [32]. More recently, we investigated partially-projecting measurements which lie somewhere between weak and projective measurement. Using random, binary, filtering

* gregory.howland.3@us.af.mil

† sknarr@ur.rochester.edu

G.A.H. and S.H.K. contributed equally to this work.

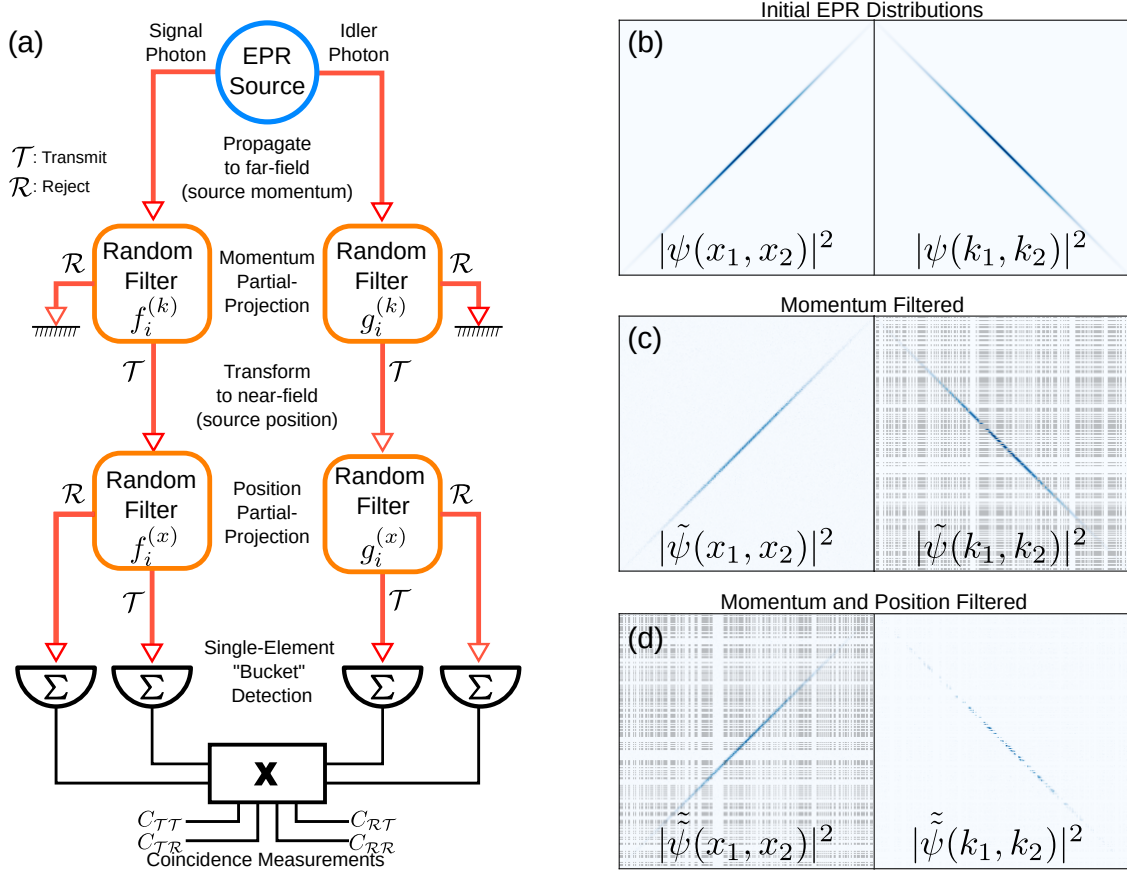


FIG. 1. **Sequential, partial-projections in position and momentum:** The block diagram (a) describes a sequence of partially-projective measurements on an EPR entangled source. (b–d) show simulated joint-position and joint-momentum distributions at each point in the experiment. Signal and idler photons from an EPR source (b) are separated and allowed to propagate to the far-field (momentum). Here they are subjected to random binary filtering by a pixelated mask (faded gray overlay). Each pixel in the mask either fully transmits (\mathcal{T}) or fully rejects (\mathcal{R}). The momentum-filtered fields (c) propagate through an optical system to an image plane of the source, where they are again filtered with random, binary filters (d). Single-element, photon-counting detectors are placed in the \mathcal{T} and \mathcal{R} ports of each filter and are connected to a coincidence circuit. The total number of coincident detection events between signal and idler channels gives a random projection of the momentum distribution. The relative distribution of coincident detections between the \mathcal{T} and \mathcal{R} modes (4 possibilities) for the signal and idler photons gives a random projection of the position distribution up to a small noise floor injected by the momentum filtering.

in position followed by strong projections in momentum, we measured the sharp image and diffraction pattern of a transverse optical field without dividing the initial ensemble, a feat impossible for strong, projective measurements [33]. With non-projective measurement, the conventional wisdom that incompatible variables must be separately investigated is discarded.

Guided by these principles, we demonstrate a novel approach for efficiently witnessing large-dimensional entanglement with a single set of measurements. We apply this technique to Einstein-Podolsky-Rosen (EPR) correlations in the spatial degrees-of-freedom of the biphoton state produced in spontaneous parametric down-conversion (SPDC), a system closely resembling the EPR *gedankenexperiment* [34, 35]. Inspired by the random measurements used in CS, we show that random, local, partial-projections in momentum followed by

random, local, partial projections in position can be used to efficiently and accurately image EPR correlations in both domains. The ensemble is not split—position and momentum measurements are performed on the same photons. Remarkably, the measurement disturbance introduced by the momentum filtering manifests as a small amount of additive noise in the position distribution, which remains un-broadened. This allows the position and momentum measurements to be decoupled, and the joint probability distributions to be recovered in a 65,536-dimensional discretization of the infinite-dimensional Hilbert space. Our measurements do not violate the uncertainty principle; rather, they highlight the complex and subtle behavior of measurement disturbance given non-projective measurements.

Exploiting our expectation that the distributions are highly correlated, we use compressive sensing optimization tech-

niques to dramatically undersample—we need fewer than 5,000 measurements to obtain high-quality distributions. By comparing the conditional Shannon entropy in the position and momentum joint distributions, we witness high-dimensional entanglement and determine a quantum secret key rate for the joint system without needing a density matrix.

I. THEORY

A. Random, partially-projective measurements of an EPR state

Consider a two-photon quantum state $|\psi\rangle$ encoded in the transverse-spatial degrees of freedom of the biphoton produced by SPDC. SPDC is a nonlinear-optical process where a high-energy pump photon is converted into two lower-energy daughter photons, labeled signal and idler. Conservation of momentum dictates that the signal and idler momenta be anti-correlated for a plane wave pump. Conservation of “birth-place”, the notion that both photons originate from the same location in the crystal, dictates positive correlations in the daughters’ transverse-positions.

Strong correlations in incompatible observables are a signature of entanglement—in fact, the original EPR paradox was described using position and momentum [34]. EPR considered the ideal state

$$\begin{aligned} |\psi\rangle &= \int dx_1 dx_2 \delta(x_1 - x_2) |x_1, x_2\rangle \\ &= \int dk_1 dk_2 \delta(k_1 + k_2) |k_1, k_2\rangle; \end{aligned} \quad (1)$$

perfectly correlated in position and perfectly anti-correlated in momentum. Although the ideal EPR state is non-normalizable and consequently impossible to realize in the lab, the biphoton state generated via SPDC is very similar [36, 37].

EPR correlations are observed by measuring the joint probability distribution in position, $|\psi(x_1, x_2)|^2$, and in momentum $|\psi(k_1, k_2)|^2$. Because these domains of interest are known in advance, only these two distributions are needed—not a full density matrix. Spatial correlations are usually measured by jointly raster scanning single-element, photon-counting detectors through either the near-field (position) or far-field (momentum) [38]. This approach scales extremely poorly with increased single-particle dimensionality n —measurement time scales between n^3 and n^4 . For a typical source, this could take upwards of one year for a modest $n = 32 \times 32$ pixel resolution [27].

To avoid dividing the ensemble, and to require many fewer measurements, we instead apply local, partially-projective measurements in momentum followed by local, partially-projective measurements in position, to the same photons. Our approach is illustrated in Fig. 1. The signal and idler photons from an EPR-like state $\psi(x_1, x_2)$ are separately allowed to propagate to the far-field. Here, each photon is locally filtered by a random, binary mask $f_i^{(k)}(k_1)$ (signal) or $g_i^{(k)}(k_2)$

(idler), where subscript i refers to a particular pair of filters. Each local filter is an n -pixel, binary intensity mask, where individual pixels fully transmit (\mathcal{T}) or fully reject (\mathcal{R}) with equal probability. The momentum filtering enacts a significant partial-projection of $|\psi\rangle$ —on average, half of the local intensity and three-quarters of the joint-intensity is rejected—so this is not a weak measurement.

All measurements are subject to uncertainty relations, which imply unavoidable measurement disturbance. Conventional projective measurements, often associated with “wave-function collapse”, localize a quantum state in one domain (e.g momentum) at the cost of broadening it in a conjugate domain (e.g. position). Critically, however, random filtering *does not localize* the quantum state; it maps a small amount of momentum information onto the total intensity passing the filter. The measurement disturbance of non-projective measurements is best understood via the entropic uncertainty principle

$$h(x) + h(k) \geq \log(\pi e), \quad (2)$$

where $h(*)$ is the Shannon entropy. The entropic uncertainty principle implies an information exclusion relation; *the more information a measurement gives about the momentum distribution, the less information a subsequent measurement can give about the position distribution* [39]. There are no restrictions, however, on how information loss manifests. In particular, a measurement in one domain need not broaden, or blur, the statistics in a complementary domain.

The joint amplitude passing the momentum-filtering is $\tilde{\psi}(k_1, k_2) = \psi(k_1, k_2) f_i^{(k)}(k_1) g_i^{(k)}(k_2)$. To see the effect of the momentum filtering on the position distribution, we take a Fourier transform to find $\tilde{\psi}(x_1, x_2) = \mathcal{F}\{\tilde{\psi}(k_1, k_2)\}$, which is given by the convolution of the state and filter functions in the position domain: $\tilde{\psi}(x_1, x_2) = \psi(x_1, x_2) \star (f_i^{(k)}(x_1) g_i^{(k)}(x_2))$. At high resolution, the Fourier transform of an n -pixel, random binary pattern is approximately proportional to $\delta(x) + \sqrt{2/n} \phi(x)$, where values for $\phi(x)$ are taken from a unit variance, complex, Gaussian noise distribution—a sharp central peak riding a small noise floor [33] (see supplemental material).

Because convolution with a delta function returns the original function, the perturbed state’s position distribution is the true distribution with some weak additive noise terms;

$$\begin{aligned} |\tilde{\psi}(x_1, x_2)|^2 &= \mathcal{N} \left| \psi(x_1, x_2) \star \right. \\ &\quad \left. \left[\left(\delta(x_1) + \sqrt{2/N} \phi_i(x_1) \right) \left(\delta(x_2) + \sqrt{2/N} \phi_i(x_2) \right) \right] \right|^2 \end{aligned} \quad (3)$$

Expanding this product in powers of $1/\sqrt{N}$, where $N = n^2$,

yields

$$\begin{aligned} |\tilde{\psi}(x_1, x_2)|^2 = \mathcal{N} \Big\{ & |\psi(x_1, x_2)|^2 \\ & + \sqrt{2/N} \text{Re} \left[\psi^*(x_1, x_2) (\psi(x_1, x_2) \star \right. \\ & \quad \left. (\delta(x_1)\phi_2(x_2) + \delta(x_2)\phi_1(x_1))) \right] \\ & \left. + \mathcal{O}(1/N) + \dots + \mathcal{O}(1/N^2) \right\} \end{aligned} \quad (4)$$

where \mathcal{N} is a normalizing constant. Remarkably, disturbance from filtering adds only a small noise floor at most a factor $\sqrt{2/N}$ weaker without otherwise broadening the position distribution. This can be seen in Fig. 1(c), where the position distribution maintains tight correlations despite the effect of momentum filtering. A rigorous derivation of equation (4), including the effect of finite width pixels, is given in the supplemental material.

Next, we again perform random filtering—this time in position—as seen in Fig. 1(d). The transmitted and rejected ports are directed to single-element “bucket” detectors that are not spatially resolving. Photon detection events are time-correlated with a coincidence circuit.

Each coincidence measurement contains information about both position and momentum; these must be decoupled to fit a measurement model

$$\begin{aligned} \mathbf{Y}^{(k)} &= \mathbf{A}\mathbf{K} + \Phi^{(k)} \\ \mathbf{Y}^{(x)} &= \mathbf{B}\mathbf{X} + \Phi^{(x)} + \Gamma^{(x)}. \end{aligned} \quad (5)$$

Here, \mathbf{K} and \mathbf{X} are N -dimensional signal vectors representing $|\psi(k_1, k_2)|^2$ and $|\psi(x_1, x_2)|^2$, and \mathbf{A} and \mathbf{B} are $M \times N$ sensing matrices. $\mathbf{Y}^{(k)}$ and $\mathbf{Y}^{(x)}$ are measurement vectors whose elements are the inner-product of \mathbf{X} or \mathbf{K} onto the i^{th} row (or sensing vector) of \mathbf{A} or \mathbf{B} . Noise vectors Φ represent additive measurement noise. Noise vector $\Gamma^{(x)}$ represents the noise injected by momentum filtering.

Momentum information is encoded in the *total* coincidences between all detection modes. Each row of \mathbf{A} is the Kronecker product of two, random single-particle sensing vectors $\mathbf{a}_i^{k_1} \otimes \mathbf{a}_i^{k_2}$ such that $\mathbf{A}_i = \mathbf{a}_i^{k_1} \otimes \mathbf{a}_i^{k_2}$, where for example $\mathbf{a}_i^{k_1}$ encodes $f_i^{(k)}(k_1)$.

Position information is encoded in the *relative* distribution of coincidences between signal and idler \mathcal{T} and \mathcal{R} modes. By adding coincidences between like-modes ($\mathcal{T}\mathcal{T}$ and $\mathcal{R}\mathcal{R}$) and subtracting coincidences between differing modes ($\mathcal{T}\mathcal{R}$ and $\mathcal{R}\mathcal{T}$), the effect of momentum filtering is removed up to injected noise. Like momentum, the position sensing vector is a Kronecker product of two local sensing vectors; $\mathbf{B}_i = \mathbf{b}_i^{(x_1)} \otimes \mathbf{b}_i^{(x_2)}$. However, because of the relative measurement, the local sensing matrices take values “1” for transmitting pixels and “-1” for rejecting pixels.

In our experiment, we use a slightly more sophisticated, but conceptually similar, approach (see supplemental material at *to be inserted*) that retains the transmission and rejection modes from both momentum and position. In this case, there

are 16 possible correlation measurements that are combined to give either position or momentum information, and both \mathbf{A} and \mathbf{B} take values “1” and “-1”.

B. Recovering the position and momentum distributions

To obtain the joint-position and joint-momentum distributions from our measurements, we turn to compressive sensing (CS). Here, we exploit our expectation that both distributions are highly correlated. Therefore, the distributions are sparse in their natural (position-pixel or momentum-pixel) representations—relatively few elements in each distribution have significant values. This allows us to dramatically under-sample so that $M \ll N$. In this case, there are many possible \mathbf{X} and \mathbf{K} consistent with the measurements. CS posits that the correct \mathbf{X} and \mathbf{K} are the sparsest distributions consistent with the measurements.

Sparse \mathbf{X} and \mathbf{K} are found by solving a pair of optimization problems

$$\begin{aligned} \min_{\mathbf{K}} \quad & \frac{\mu_k}{2} \|\mathbf{Y}^{(k)} - \mathbf{A}\mathbf{K}\|_2^2 + TV(\mathbf{K}) \\ \min_{\mathbf{X}} \quad & \frac{\mu_x}{2} \|\mathbf{Y}^{(x)} - \mathbf{B}\mathbf{X}\|_2^2 + TV(\mathbf{X}), \end{aligned} \quad (6)$$

where $\|\cdot\|_2$ is the ℓ_2 (Euclidean) norm, and μ are weighting constants. The first penalty is a least-squares term that ensures the result is consistent with measured data. The second penalty, $TV(\cdot)$, is the signal’s total variation (TV), which is the ℓ_1 norm of the discrete gradient

$$TV(\mathbf{X}) = \sum_{\text{adj. } i,j} |\mathbf{X}_i - \mathbf{X}_j|, \quad (7)$$

where i, j run over pairs of adjacent elements in the signal. The TV regularization promotes structured, sparse signals over noisy, uncorrelated signals. Total variation minimization has been extremely successful for compressed sensing and denoising in the context of imaging [40–42]. In many cases, a signal can be recovered from M as low as a few percent of N . For a more complete introduction to compressive sensing, see excellent tutorials by Baraniuk [43] and Candès and Wakin [44].

Total variation minimization is also extremely effective for denoising signals [45]. Normally, this helpfully mitigates environmental and photon-counting shot noise (Φ), but in our case also largely removes the filtering measurement disturbance Γ . With strong measurements, e.g. raster-scanning a pinhole aperture, one requires deconvolution techniques to obtain a similar effect. Not only is deconvolution far more challenging than denoising, it can never recover high frequency content beyond the aperture size.

CS measurements are most effective in a representation that is incoherent, or maximally unbiased, with respect to the sparse representations (in our case position or momentum). Fortunately, random projections perfectly suit this criteria, leading to the surprising conclusion that random measurement is actually preferable. Random matrices are overwhelmingly likely to be restricted isometries that preserve the

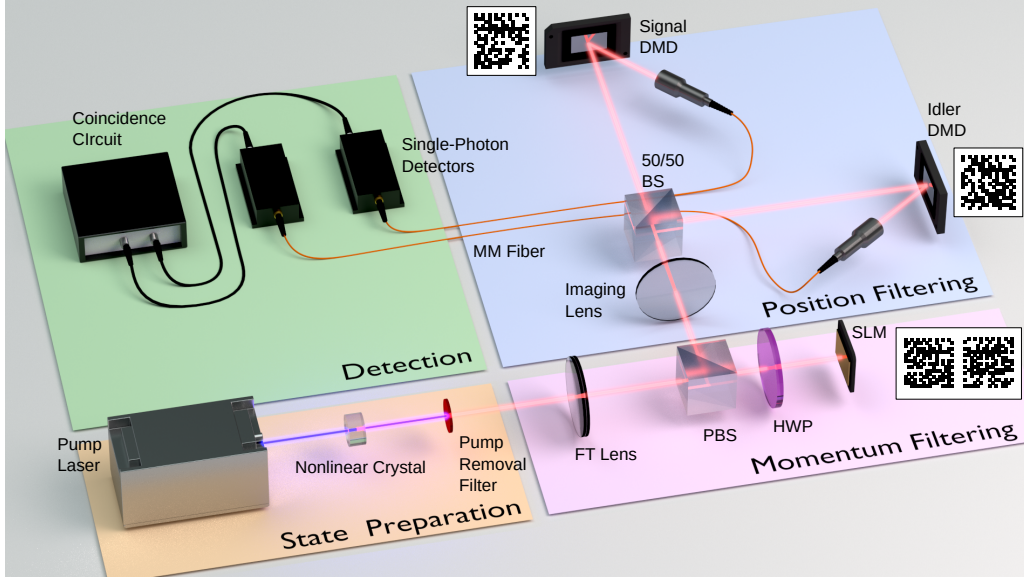


FIG. 2. **Experimental Setup:** A two-photon, EPR-like state is generated by pumping a nonlinear crystal for Type-1 SPDC. Random, binary patterns placed on an SLM in a Fourier plane of the crystal and on DMDs in an image plane of the crystal implement a sequence of random, partially-projecting measurements. Example patterns are shown next to the SLM and DMDs; note the separate patterns for signal and idler photons on the SLM. Coincident detection events between single-photon detectors for signal and idler photons give information about *both* the joint-position and joint-momentum distributions of the two-photon state.

relative distance between sparse signals, ensuring that solving Eq. 6 returns the true signal instead of a sparse but otherwise incorrect result [46]. Not only do random filters extract information in complementary domains, they are among the best measurements for leveraging CS.

One might reasonably ask if our technique employs circular reasoning—assuming the distributions are highly correlated in order to then measure their correlations. This is not the case. The initial assumption is a compressibility assumption; relative to all possible distributions, our distributions are expected to be sparse in the natural pixel basis. We do not know exactly how sparse the distributions will be, or which elements will be significant. However, the vast majority of possible distributions are just unstructured noise—these are the outcomes we are initially rejecting.

The assumption is similar to assuming a digital photograph can be effectively compressed by the JPEG standard [47]. A natural photographic scene contains more low-spatial-frequency content than high-spatial-frequency content and contains objects with well defined edges and recognizable shapes—regardless of the specific scene.

II. EXPERIMENT

Our experimental setup is shown in Fig. 2. An EPR-like state at 810 nm is generated by pumping a 1 mm thick BiBO crystal oriented for Type-I, collinear SPDC with a 405 nm pump laser. The generated fields propagate to a spatial light modulator (SLM) in the focal plane of a 125 mm lens. Because the phase-only SLM only retards one polarization, it can perform per-pixel polarization rotation. These polariza-

tion rotations are converted to intensity modulations with a half-wave plate and a polarizing beamsplitter. Random masks which cause zero or π polarization rotations perform the momentum filtering. We exploit the negative correlations in the momentum state to assign signal and idler particles to the left- and right-halves of the SLM respectively.

The signal and idler fields are routed to separate digital micromirror devices (DMDs) via a 500 mm lens and 50/50 beamsplitter; the DMDs are placed in a crystal image plane with 4X magnification. A DMD is a two-dimensional array of individually addressable mirrors, each of which can be oriented to direct light towards or away from a detector. These correspond to the transmit and reject ports in Fig. 1. Random patterns placed on the DMDs implement the position filtering. The light is coupled with 10X microscope objectives into multi-mode fibers which are connected to avalanche photo-diodes operating in Geiger (photon-counting) mode. A correlator records coincident detection events between filtered signal and idler photons.

Single-particle sensing matrices $\mathbf{a}^{(k_1)}$, $\mathbf{a}^{(k_2)}$, $\mathbf{b}^{(x_1)}$, and $\mathbf{b}^{(x_2)}$ are generated by taking M rows from randomly permuted $n \times n$ Hadamard matrices. This allows the repeated calculations of \mathbf{AK} and \mathbf{BX} performed by the solver to use a Fast Hadamard transform, decreasing computational requirements [48]. Because we only collect transmitted modes from both position and momentum filters, we require 16 separate measurements to collect all coincident combinations of transmission and rejection for the 4 filters (described in supplemental material). This is not required in principle if one has 8 detectors. The solver we use for equation (6) is TVAL3 [49]. The full measurement and reconstruction recipe we follow is similar to that described in Ref. [48].

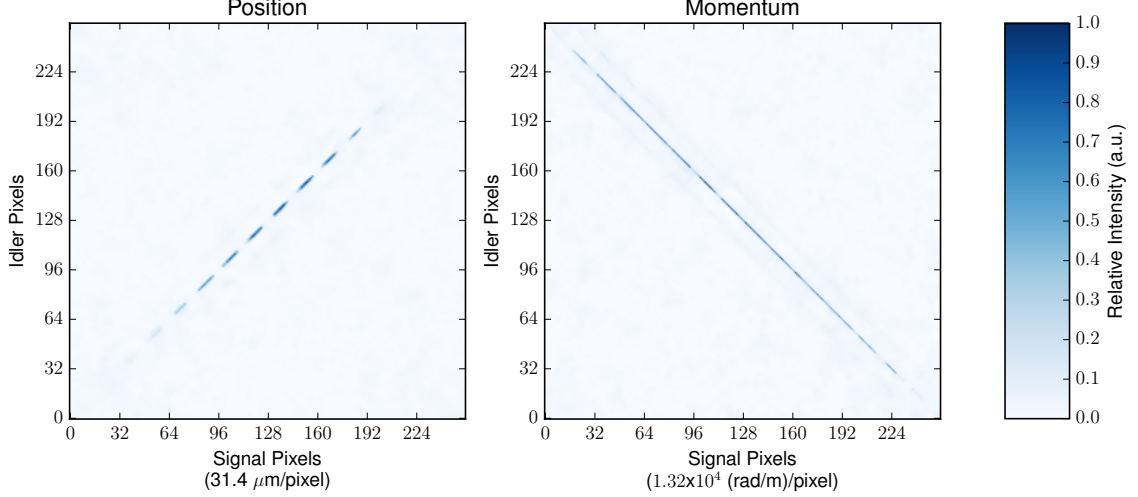


FIG. 3. **Representative recovered joint-position and joint-momentum signals.** Recovered joint-position and joint-momentum signals for a 16×16 pixel ($N = 256 \times 256$) discretization. Only $M = 4,439$ measurements were needed, about $0.07N$. Gaps along the position diagonal occur due to reshaping to one dimension—these regions were outside the marginal width. Position and momentum units refer to the transverse plane at the nonlinear crystal ($z = 0$).

Note that our choice of a single momentum SLM and two position DMDs was due to available equipment. One would ideally use four SLMs to implement completely separate position and momentum filtering for both the signal and idler fields. The SLM is preferred for filtering because of its high ($> 90\%$) diffraction efficiency in contrast to the lower ($\approx 20\%$) diffraction efficiency for the DMDs.

III. RESULTS

A. Signal Recovery

Sample recovered joint signals for position and momentum are given in Fig. 3 as returned directly by the solver. The single-particle resolution was $n = 16 \times 16$ pixels, so the joint signal has dimensionality $N = n^2 = 65,536$. For the sample image, $M = 4,439$ random projections were used corresponding to M less than $0.07N$. Positive correlations in position and negative correlations in momentum between signal and idler particles are clearly seen. The gaps visible on the diagonal are an artifact of row-wise reshaping to one-dimension—these regions are physically outside the marginal beam width.

B. Reconstruction Noise

Unfortunately, the images shown in Fig. 3 do not represent valid probability distributions due to the presence of weak, zero-mean, additive noise shown in Fig. 4. Note that the objective function, Eq. 6, does not restrict to valid probability distributions and allows negative values. We found that

current, established solvers such as TVAL3 performed better without such additional constraints—improved, quantum-specific solvers are a topic of future research.

Fig. 4(a) shows slices of the joint-position reconstruction along the signal axis, where each curve corresponds to a particular idler pixel. Zooming in on a region with no signal in Fig. 4(b), we observe the noise. This noise contains both measurement uncertainty and solver artifacts. Potential noise sources include shot-noise, long term drift in the pump laser, stray light, and crystal temperature instability. Fig. 4(c) gives a histogram of the noise shown in Fig. 4(b) which follows Gaussian statistics. An appropriate model for signals returned by the solver is therefore

$$\mathbf{X}^{(r)} = \mathbf{X} + \mathbf{G}^{(x)} \quad (8)$$

$$\mathbf{K}^{(r)} = \mathbf{K} + \mathbf{G}^{(k)}, \quad (9)$$

where $\mathbf{X}^{(r)}$ and $\mathbf{K}^{(r)}$ refer to the signals returned by the solver and $\mathbf{G}^{(x)}$ and $\mathbf{G}^{(k)}$ are additive, zero-mean Gaussian noise.

The simplest way to obtain valid probability distributions is to threshold values below a small percentage of the maximum value to zero. As seen in Fig. 4(b), any threshold below 5% removes the uniform noise floor without removing any signal peaks. This approach is similar to the common technique of subtracting dark counts from data in coincidence measurements and other noise suppression techniques.

C. Witnessing entanglement

To witness and quantify entanglement, we violate an entropic steering inequality [50–52] (see supplemental mate-

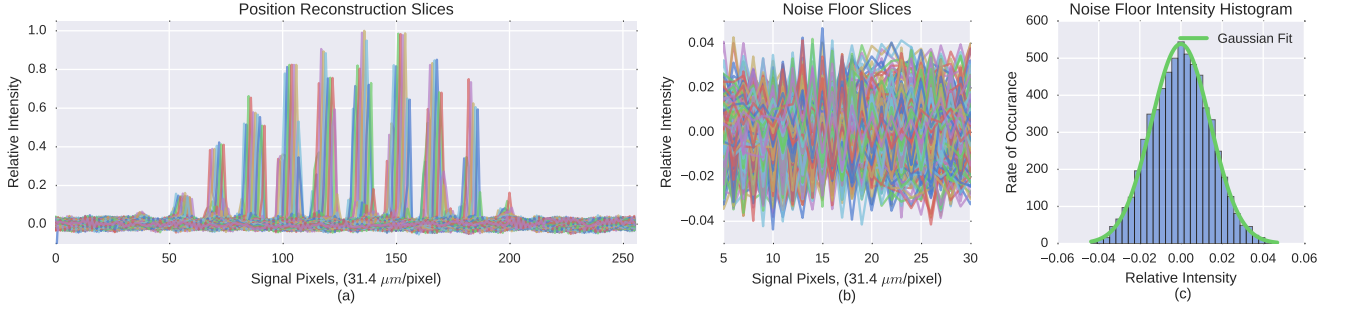


FIG. 4. **Reconstruction noise:** One-dimensional slices along the signal axis of the joint-position reconstruction from Fig. 3 in (a) reveal the presence of zero-mean, additive Gaussian noise. The presence of negative values strongly suggests this noise’s form is non-physical; the reconstruction process maps measurement uncertainty into this noise. A close-up of a noise-only region (signal pixels 5 to 30, all idler pixel spectra) is shown in (b). A histogram of outcomes (c) for the region shown in (b) demonstrates that the noise follows Gaussian statistics with zero mean and standard deviation .014 . To obtain a valid probability distribution, values below a chosen threshold can be set to zero and the distribution normalized.

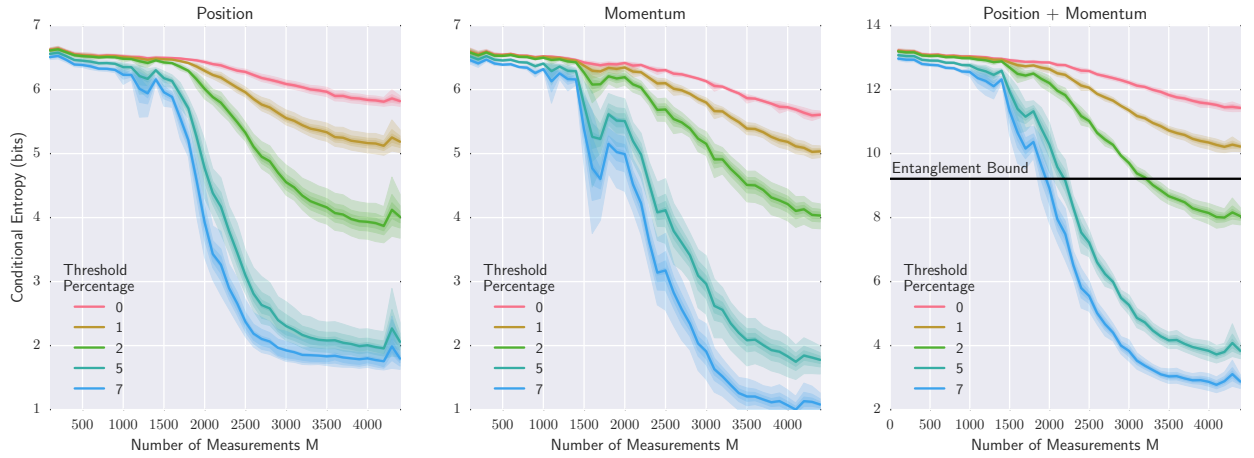


FIG. 5. **Conditional entropy versus measurement number:** A sharp transition from high to low conditional entropy is seen as the number of measurements increases. Note that $N = 256^2$, so $M = 2,000$ is only $.03N$. Different curves correspond to different levels of thresholding to remove the noise floor. Bold lines indicate an average over for 9 trials. Faded lines enclose up to four standard deviations about the mean. When the conditional entropy sum is below the bound, the state is entangled.

rial); all classically correlated states satisfy

$$H(X_1|X_2) + H(K_1|K_2) \geq 2 \log \left(\frac{\pi e}{\Delta_x \Delta_k} \right), \quad (10)$$

where $H(X_1|X_2)$ and $H(K_1|K_2)$ are the conditional, discrete Shannon entropies of the respective position and momentum joint-distributions. Δ_k (Δ_x) is the width in momentum (position) sampled by a single pattern pixel on the SLM (DMD) in the transverse plane of the nonlinear crystal. For position Δ_x , this is found by dividing the physical width of a pattern pixel on the DMD by the magnification of the imaging system. For momentum, the physical width of an SLM pattern pixel p_k is related to Δ_k via the Fourier transforming property of a lens, so $\Delta_k = p_k 2\pi / (\lambda f)$, where λ is the wavelength of light and f is the lens focal length.

The entropic steering inequality is powerful because it is computed directly from measured probability distributions and does not require a density matrix. Remarkably, despite being a function of discrete distributions, it witnesses

continuous-variable entanglement. Moreover, the amount the inequality is violated corresponds to a secret key rate for quantum key distribution [53, 54].

The conditional entropies in position and momentum for our experimental results are given in Fig. 5 as a function of measurement number. Different curves correspond to increased levels of thresholding, setting values below a percentage of the maximum value to 0. A sharp transition from poor reconstruction to good reconstruction is clearly demonstrated by dramatic drops in the conditional entropies around $M = 2,000$. This transition is characteristic of compressed sensing as the number of measurements becomes sufficient to accurately reconstruct the signal [55]—strongly suggesting we made enough measurements. For too small M , reconstructions fail spectacularly and return unstructured noise. For a k -sparse signal (k out of N elements have significant intensity), the required number of measurements scales as $ck \log(N/k)$ where c is a near-unity constant [21]. For M beyond the transition, one is sampling at above the information rate. Tra-

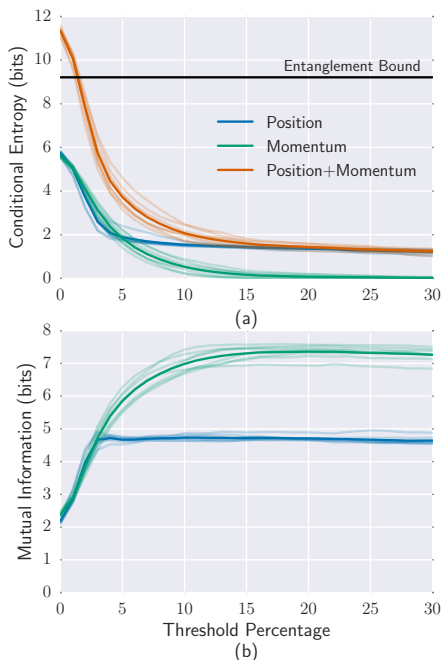


FIG. 6. **Effect of thresholding:** The effect of thresholding to remove weak background noise on the conditional entropy (a) and mutual information (b) is given. The bold line gives the average for 9 trials, faded lines give the results from the individual trials. $M = 4,439$ measurements were used. When the conditional entropy sum is below the bound, the state is entangled.

ditionally one is concerned with sampling at or beyond the Nyquist rate where $M = N$.

In momentum, the conditional entropy drops to nearly zero; in position it drops to less than 2 bits. The position entropy likely levels off due to slight pixel-misalignment between the two position DMDs. Physically, this indicates a particular signal position pixel is correlated to about four idler pixels, whereas a particular signal momentum pixel is only correlated to one idler pixel. The steering inequality is violated with as little as 2 percent thresholding, and by over 6 bits for thresholding beyond 7 percent.

The effect of thresholding for $M = 5,000$ is given in Fig. 6. Fig. 6(a) shows the conditional entropies for position, momentum, and their sum with the corresponding entanglement bound. Fig. 6(b) gives the mutual informations $I(X_1 : X_2)$ and $I(K_1 : K_2)$, where for example

$$I(X_1 : X_2) = H(X_1) + H(X_2) - H(X_1, X_2). \quad (11)$$

Here, $H(X_1, X_2)$ is the Shannon entropy of the joint distribution and $H(X_1)$ and $H(X_2)$ are Shannon entropies of the marginal, single particle distributions. From information the-

ory, these mutual informations provide a maximum bit-rate for communication with joint-position or joint-momentum representations for this system [56]. The mutual information rises as a function of thresholding, indicating that thresholding is not trivially decreasing the conditional entropies and that the most likely joint-outcomes are the most highly correlated. Again, the momentum mutual information is larger due to slight optical misalignments for position DMDs.

An important point is that the thresholded signal peaks still retain the additive Gaussian noise from the reconstruction process. Due to the data processing inequality [56], this noise cannot decrease the conditional entropy and cannot increase the mutual information (this would be like arguing a noisy channel is better for communication than its noiseless counterpart). Therefore, we conservatively underestimate our ability to violate the steering witness (Eq. A16).

IV. CONCLUSION

We have demonstrated that local, random filtering in momentum followed by local, random filtering in position—of the same photons—can recover sharp, joint distributions for both observables. This is not possible with standard, projective measurements that localize photons in either position or momentum. Using the expectation that the signals will be highly correlated allows us to use many fewer measurements than dimensions in the system via techniques of compressed sensing. We strongly emphasize that we have not violated any uncertainty relations; instead, we have chosen non-projective measurements whose disturbance can easily be mitigated.

V. ACKNOWLEDGMENTS

This work was funded by Air Force Office of Scientific Research (AFOSR) Grant No. FA9550-13-1-0019 and AFOSR LRIR 14RI02COR. G. A. H. and J. S. acknowledge support from National Research Council Research Associate Programs. J. C. H. acknowledges support from Northrup Grumman. Any opinions, findings and conclusions or recommendations expressed in this material are those of the author(s) and do not necessarily reflect the views of AFRL.

G. A. H. conceived of the experiment and authored the manuscript with help from S. H. K., D. J. L., and J. S. S. H. K. and G. A. H. performed the experiment and analyzed the data. J. S. provided the theory on entanglement witnesses and Fourier transforms of random patterns. D. J. L. devised the scheme for using Hadamard matrices in the measurement and reconstruction process. The entire project was overseen by J. C. H. G. A. H. and S. H. K. contributed equally to the work presented in this manuscript.

[1] Matteo Paris and Jaroslav Rehacek, *Quantum state estimation*, Vol. 649 (Springer Science & Business Media, 2004).

[2] Gregor Weihs, Thomas Jennewein, Christoph Simon, Harald Weinfurter, and Anton Zeilinger, “Violation of bell’s inequality

- under strict einstein locality conditions,” *Phys. Rev. Lett.* **81**, 5039–5043 (1998).
- [3] Lee A. Rozema, Dylan H. Mahler, Alex Hayat, Peter S. Turner, and Aephraim M. Steinberg, “Quantum data compression of a qubit ensemble,” *Phys. Rev. Lett.* **113**, 160504 (2014).
 - [4] RT Thew, Kae Nemoto, Andrew G White, and William J Munro, “Qudit quantum-state tomography,” *Physical Review A* **66**, 012303 (2002).
 - [5] Andreas Klappenecker and Martin Rötteler, “Constructions of mutually unbiased bases,” in *Finite fields and applications* (Springer, 2004) pp. 137–144.
 - [6] A. I. Lvovsky and M. G. Raymer, “Continuous-variable optical quantum-state tomography,” *Rev. Mod. Phys.* **81**, 299–332 (2009).
 - [7] Scott Aaronson, “The learnability of quantum states,” *Proceedings of the Royal Society A: Mathematical, Physical and Engineering Science* **463**, 3089–3114 (2007).
 - [8] Irfan Ali-Khan, Curtis J. Broadbent, and John C. Howell, “Large-alphabet quantum key distribution using energy-time entangled bipartite states,” *Phys. Rev. Lett.* **98**, 060503 (2007).
 - [9] Ryszard Horodecki, Paweł Horodecki, Michał Horodecki, and Karol Horodecki, “Quantum entanglement,” *Rev. Mod. Phys.* **81**, 865–942 (2009).
 - [10] Eric Gama Cavalcanti, Steve James Jones, Howard Mark Wiseman, and Margaret D Reid, “Experimental criteria for steering and the einstein-podolsky-rosen paradox,” *Physical Review A* **80**, 032112 (2009).
 - [11] Z Hradil, “Quantum-state estimation,” *Physical Review A* **55**, R1561 (1997).
 - [12] Daniel F. V. James, Paul G. Kwiat, William J. Munro, and Andrew G. White, “Measurement of qubits,” *Phys. Rev. A* **64**, 052312 (2001).
 - [13] Carlton M Caves, Christopher A Fuchs, and Rüdiger Schack, “Quantum probabilities as bayesian probabilities,” *Physical review A* **65**, 022305 (2002).
 - [14] Ferenc Huszár and Neil MT Houlsby, “Adaptive bayesian quantum tomography,” *Physical Review A* **85**, 052120 (2012).
 - [15] D.L. Donoho, “Compressed sensing,” *Information Theory, IEEE Transactions on* **52**, 1289–1306 (2006).
 - [16] Igor Carron, “Compressive sensing: The big picture,” <http://sites.google.com/site/igorcarron2/cs> (2009).
 - [17] Marco F Duarte, Mark A Davenport, Dharmpal Takhar, Jason N Laska, Ting Sun, Kevin E Kelly, Richard G Baraniuk, *et al.*, “Single-pixel imaging via compressive sampling,” *IEEE Signal Processing Magazine* **25**, 83 (2008).
 - [18] Justin Romberg, “Imaging via compressive sampling [introduction to compressive sampling and recovery via convex programming],” *IEEE Signal Processing Magazine* **25**, 14–20 (2008).
 - [19] Baoqing Sun, Matthew P Edgar, Richard Bowman, Liberty E Vittert, Stuart Welsh, A Bowman, and MJ Padgett, “3d computational imaging with single-pixel detectors,” *Science* **340**, 844–847 (2013).
 - [20] Ahmed Kirmani, Dheera Venkatraman, Donggeek Shin, Andrea Colaço, Franco NC Wong, Jeffrey H Shapiro, and Vivek K Goyal, “First-photon imaging,” *Science* **343**, 58–61 (2014).
 - [21] E.J. Candes, J. Romberg, and T. Tao, “Robust uncertainty principles: exact signal reconstruction from highly incomplete frequency information,” *Information Theory, IEEE Transactions on* **52**, 489–509 (2006).
 - [22] David Gross, Yi-Kai Liu, Steven T Flammia, Stephen Becker, and Jens Eisert, “Quantum state tomography via compressed sensing,” *Physical review letters* **105**, 150401 (2010).
 - [23] A Shabani, M Mohseni, S Lloyd, RL Kosut, and H Rabitz, “Estimation of many-body quantum hamiltonians via compressive sensing,” *Physical Review A* **84**, 012107 (2011).
 - [24] Wei-Tao Liu, Ting Zhang, Ji-Ying Liu, Ping-Xing Chen, and Jian-Min Yuan, “Experimental quantum state tomography via compressed sampling,” *Phys. Rev. Lett.* **108**, 170403 (2012).
 - [25] Francesco Tonolini, Susan Chan, Megan Agnew, Alan Lindsay, and Jonathan Leach, “Reconstructing high-dimensional two-photon entangled states via compressive sensing,” *Scientific reports* **4** (2014).
 - [26] Christian Schwemmer, Géza Tóth, Alexander Niggebaum, Tobias Moroder, David Gross, Otfried Gühne, and Harald Weinfurter, “Experimental comparison of efficient tomography schemes for a six-qubit state,” *Phys. Rev. Lett.* **113**, 040503 (2014).
 - [27] Gregory A. Howland and John C. Howell, “Efficient high-dimensional entanglement imaging with a compressive-sensing double-pixel camera,” *Phys. Rev. X* **3**, 011013 (2013).
 - [28] Amir Kalev, Robert L. Kosut, and Ivan H. Deutsch, “Quantum tomography protocols with positivity are compressed sensing protocols,” *Npj Quantum Information* **1**, 15018 EP – (2015), article.
 - [29] Justin Dressel, Mehul Malik, Filippo M Miatto, Andrew N Jordan, and Robert W Boyd, “Colloquium: Understanding quantum weak values: Basics and applications,” *Reviews of Modern Physics* **86**, 307 (2014).
 - [30] Jeff S Lundeen, Brandon Sutherland, Aabid Patel, Corey Stewart, and Charles Bamber, “Direct measurement of the quantum wavefunction,” *Nature* **474**, 188–191 (2011).
 - [31] Sacha Kocsis, Boris Braverman, Sylvain Ravets, Martin J Stevens, Richard P Mirin, L Krister Shalm, and Aephraim M Steinberg, “Observing the average trajectories of single photons in a two-slit interferometer,” *Science* **332**, 1170–1173 (2011).
 - [32] TC White, JY Mutus, J Dressel, J Kelly, R Barends, E Jeffrey, D Sank, A Megrant, B Campbell, Yu Chen, *et al.*, “Violating the bell-leggett-garg inequality with weak measurement of an entangled state,” *arXiv preprint arXiv:1504.02707* (2015).
 - [33] Gregory A. Howland, James Schneeloch, Daniel J. Lum, and John C. Howell, “Simultaneous measurement of complementary observables with compressive sensing,” *Phys. Rev. Lett.* **112**, 253602 (2014).
 - [34] Albert Einstein, Boris Podolsky, and Nathan Rosen, “Can quantum-mechanical description of physical reality be considered complete?” *Physical review* **47**, 777 (1935).
 - [35] John C. Howell, Ryan S. Bennink, Sean J. Bentley, and R. W. Boyd, “Realization of the einstein-podolsky-rosen paradox using momentum- and position-entangled photons from spontaneous parametric down conversion,” *Phys. Rev. Lett.* **92**, 210403 (2004).
 - [36] Stephen P Walborn, CH Monken, S Pádua, and PH Souto Ribeiro, “Spatial correlations in parametric down-conversion,” *Physics Reports* **495**, 87–139 (2010).
 - [37] James Schneeloch and John C Howell, “Introduction to the transverse spatial correlations in spontaneous parametric down-conversion through the biphoton birth zone,” *Journal of Optics* **18**, 053501 (2016).
 - [38] Malcolm N OSullivan-Hale, Irfan Ali Khan, Robert W Boyd, and John C Howell, “Pixel entanglement: experimental realization of optically entangled $d=3$ and $d=6$ qudits,” *Physical review letters* **94**, 220501 (2005).
 - [39] Michael JW Hall, “Information exclusion principle for complementary observables,” *Physical review letters* **74**, 3307 (1995).
 - [40] Xianbiao Shu and Narendra Ahuja, “Hybrid compressive sampling via a new total variation tv11,” in *Computer Vision—ECCV 2010* (Springer, 2010) pp. 393–404.

- [41] Antonin Chambolle and Pierre-Louis Lions, “Image recovery via total variation minimization and related problems,” *Numerische Mathematik* **76**, 167–188 (1997).
- [42] Chengbo Li, *An efficient algorithm for total variation regularization with applications to the single pixel camera and compressive sensing*, Ph.D. thesis, Citeseer (2009).
- [43] Richard G Baraniuk, “Compressive sensing,” *IEEE signal processing magazine* **24** (2007).
- [44] Emmanuel J Candès and Michael B Wakin, “An introduction to compressive sampling,” *Signal Processing Magazine, IEEE* **25**, 21–30 (2008).
- [45] Leonid I Rudin, Stanley Osher, and Emad Fatemi, “Nonlinear total variation based noise removal algorithms,” *Physica D: Nonlinear Phenomena* **60**, 259–268 (1992).
- [46] Emmanuel J Candès, “The restricted isometry property and its implications for compressed sensing,” *Comptes Rendus Mathematique* **346**, 589–592 (2008).
- [47] Gregory K Wallace, “The jpeg still picture compression standard,” *Communications of the ACM* **34**, 30–44 (1991).
- [48] Daniel J. Lum, Samuel H. Knarr, and John C. Howell, “Fast hadamard transforms for compressive sensing of joint systems: measurement of a 3.2 million-dimensional bi-photon probability distribution,” *Opt. Express* **23**, 27636–27649 (2015).
- [49] Chengbo Li, Wotao Yin, and Yin Zhang, “Users guide for tval3: Tv minimization by augmented lagrangian and alternating direction algorithms,” CAAM report (2009).
- [50] H. M. Wiseman, S. J. Jones, and A. C. Doherty, “Steering, entanglement, nonlocality, and the einstein-podolsky-rosen paradox,” *Phys. Rev. Lett.* **98**, 140402 (2007).
- [51] S. P. Walborn, A. Salles, R. M. Gomes, F. Toscano, and P. H. Souto Ribeiro, “Revealing hidden einstein-podolsky-rosen non-locality,” *Phys. Rev. Lett.* **106**, 130402 (2011).
- [52] James Schneeloch, P. Ben Dixon, Gregory A. Howland, Curtis J. Broadbent, and John C. Howell, “Violation of continuous-variable einstein-podolsky-rosen steering with discrete measurements,” *Phys. Rev. Lett.* **110**, 130407 (2013).
- [53] Cyril Branciard, Eric G. Cavalcanti, Stephen P. Walborn, Valerio Scarani, and Howard M. Wiseman, “One-sided device-independent quantum key distribution: Security, feasibility, and the connection with steering,” *Phys. Rev. A* **85**, 010301 (2012).
- [54] James Schneeloch, Samuel H. Knarr, Gregory A. Howland, and John C. Howell, “Demonstrating continuous variable einstein-podolsky-rosen steering in spite of finite experimental capabilities using fano steering bounds,” *J. Opt. Soc. Am. B* **32**, A8–A14 (2015).
- [55] Surya Ganguli and Haim Sompolsky, “Statistical mechanics of compressed sensing,” *Physical review letters* **104**, 188701 (2010).
- [56] Thomas M Cover and Joy A Thomas, *Elements of information theory* (John Wiley & Sons, 2012).
- [57] David L Donoho, Arian Maleki, and Andrea Montanari, “The noise-sensitivity phase transition in compressed sensing,” *Information Theory, IEEE Transactions on* **57**, 6920–6941 (2011).
- [58] James Schneeloch, Curtis J Broadbent, Stephen P Walborn, Eric G Cavalcanti, and John C Howell, “Einstein-podolsky-rosen steering inequalities from entropic uncertainty relations,” *Physical Review A* **87**, 062103 (2013).

Appendix A: Supplemental Material

1. Fourier transform of a random, binary filter

Let q and p be complementary variables where functions in q and p are related by a Fourier transform. q represents the domain being filtered (in our case, momentum). A local, random, N -pixel filter in q can be represented as a sum of n top-hat pixel functions arranged on a regular lattice, each multiplied by zero or unity with probability $1/2$;

$$f_i(q) = \sum_l a_l^{(i)} \prod_W (q - Wl/2), \quad (\text{A1})$$

where W is the width of a pixel. Taking the Fourier transform, we obtain

$$f_i(p) = \frac{W}{\sqrt{2\pi}} \text{Env}(p) \times \sum_l a_l^{(i)} e^{-iWlp/2}, \quad (\text{A2})$$

where the envelope $\text{Env}(p)$ is

$$\text{Env}(p) = \text{Sinc} \left(\frac{Wp}{2} \right). \quad (\text{A3})$$

For small W , as with a high resolution pattern in a small window, $\text{Env}(p)$ is broad and nearly uniform.

For large N , the summation term in Eq. (A2) can be modeled as a sum of $N/2$ phasors of unit length. At $p = 0$, the phasors add in phase so the $p = 0$ component is $N/2$. Because the nonzero elements of $a^{(i)}$ are randomly distributed, values of $f(p)$ for $p \neq 0$ can be modeled as a sum of $N/2$ randomly oriented unit-length, phasors modulated by $\text{Env}(p)$. This sum is effectively a two-dimensional random walk in the complex plane. For large values of N typical in imaging, the resulting sampling distribution is a circularly-symmetric Gaussian distribution in the complex plane.

A model for $f(p)$ is therefore,

$$f(p) = \frac{N}{2} \text{Env}(p) \left(\delta(p) + \sqrt{\frac{2}{N}} \phi_i(p) \right), \quad (\text{A4})$$

where values for $\phi_i(p)$ are complex numbers with uniformly varying phase and square magnitude distributed according to a χ^2 distribution with standard deviation $\sigma = \sqrt{1/2}$ so $\langle |\phi_i(p)|^2 \rangle = 1$ and $\langle \cdot \rangle$ is an average over many filter functions.

The end result is effectively a large delta function at $p = 0$ riding a small noise floor a factor $\sqrt{N/2}$ weaker, all modulated by a envelope function given by the width of a pixel in q .

2. Effect of random, partial projections in the complementary domain

Consider filtering a bipartite wavefunction $\psi(q_1, q_2)$ with random local filters $f_i(q_1)$ and $g_i(q_2)$, which is the product

$$\tilde{\psi}(q_1, q_2) = \psi(q_1, q_2) f_i(q_1) g_i(q_2). \quad (\text{A5})$$

The effect of filtering in the complementary domain is found by taking the Fourier transform of Eq. A5. Because the product of two functions in one domain is a convolution in the complementary domain, we find

$$\tilde{\psi}(p_1, p_2) = \mathcal{F} \{ \psi(q_1, q_2) f_i(q_1) g_i(q_2) \} \quad (\text{A6})$$

$$= \mathcal{N} \psi(p_1, p_2) \star \left[\left(\delta(p_1) + \sqrt{2/N} \phi_i(p_1) \right) \left(\delta(p_2) + \sqrt{2/N} \phi_i(p_2) \right) \right], \quad (\text{A7})$$

where \mathcal{N} is a normalization constant, envelope functions $\text{Env}(p)$ are assumed to be uniform, and \star denotes convolution. Because convolution with a δ -function returns the original function, this result will give the true momentum distribution plus a series of weak, additive noise terms. It is convenient to expand in powers of $1/\sqrt{N}$ to give

$$\begin{aligned} |\tilde{\psi}(p_1, p_2)|^2 &= \mathcal{N} \left[|\psi(p_1, p_2)|^2 \right. \\ &\quad + \frac{2\sqrt{2}}{\sqrt{N}} \text{Re}[\psi^*(p_1, p_2) (\psi(p_1, p_2) \star (\delta(p_1)\phi_j(p_2)) + \delta(p_2)\phi_i(p_1))] \\ &\quad + \frac{4}{N} \text{Re}[\psi^*(p_1, p_2) (\psi(p_1, p_2) \star (\phi_i(p_1)\phi_j(p_2))] \\ &\quad + \frac{2}{N} |\psi(p_1, p_2) \star (\delta(p_1)\phi_j(p_2)) + \delta(p_2)\phi_i(p_1)|^2 \\ &\quad + \frac{2^{\frac{5}{2}}}{N^{\frac{3}{2}}} \text{Re}[(\psi^*(p_1, p_2) \star (\delta(p_1)\phi_j^*(p_2)) + \delta(p_2)\phi_i^*(p_1)) \star \\ &\quad \star (\psi(p_1, p_2) \star \phi_i(p_1)\phi_j(p_2))] \\ &\quad \left. + \frac{4}{N^2} |\psi(p_1, p_2) \star \phi_i(p_1)\phi_j(p_2)|^2 \right], \quad (\text{A8}) \end{aligned}$$

When averaging over many patterns, coherent interference terms average to zero, yielding the simpler expression

$$\begin{aligned} \langle |\tilde{\psi}(p_1, p_2)|^2 \rangle &\approx \mathcal{N}' \left[|\psi(p_1, p_2)|^2 \right. \\ &\quad + \frac{2}{N} |\psi(p_1, p_2) \star (\delta(p_1)\phi_j(p_2)) + \delta(p_2)\phi_i(p_1)|^2 \\ &\quad \left. + \frac{4}{N^2} |\psi(p_1, p_2) \star \phi_i(p_1)\phi_j(p_2)|^2 \right], \quad (\text{A9}) \end{aligned}$$

where $\langle \cdot \rangle$ is an average over many filter functions.

3. Full measurement process

In order to measure the interaction of the light with a single set of random patterns, one needs 16 different coincidence measurements corresponding to all combinations for the transmitting and rejection ports for each filter. These can be performed simultaneously with 8 detectors. However, because we had only two detectors, we performed them in sequence. These measurements must be combined to decouple position from momentum and fit the linear measurement model.

$$\mathbf{Y}^{(k)} = \mathbf{A}\mathbf{K} + \mathbf{\Phi}^{(k)} \quad (\text{A10})$$

$$\mathbf{Y}^{(x)} = \mathbf{B}\mathbf{X} + \mathbf{\Phi}^{(x)} + \mathbf{\Gamma}^{(x)}. \quad (\text{A11})$$

Here, \mathbf{X} and \mathbf{K} are N -dimensional signal vectors representing $|\psi(x_1, x_2)|^2$ and $|\psi(k_1, k_2)|^2$, \mathbf{A} and \mathbf{B} are $M \times N$ sensing matrices, $\mathbf{\Phi}$ are M -dimensional noise vectors. $\mathbf{\Gamma}^{(x)}$ is the extra noise injected into the \mathbf{X} signal by first filtering in \mathbf{K} . $\mathbf{Y}^{(k)}$ and $\mathbf{Y}^{(x)}$ are measurement vectors whose elements are inner-products of \mathbf{X} or \mathbf{K} with the i^{th} row (or sensing vector) of \mathbf{A} or \mathbf{B} . $\mathbf{\Gamma}^{(x)}$ is a noise vector representing the noise introduced as a consequence of filtering in momentum.

An N -dimensional sensing vector, e.g. \mathbf{A}_i , consists of the Kronecker product of two n -dimensional, single-particle sensing vectors such that $\mathbf{A}_i = \mathbf{a}_i^{(k_1)} \otimes \mathbf{a}_i^{(k_2)}$. The elements of $\mathbf{a}_i^{(k_1)}$ and $\mathbf{a}_i^{(k_2)}$ randomly take values “1” (transmit) and “-1” (reject) with equal probability. A similar process defines single-particle sensing vectors \mathbf{b} in position.

There are therefore 16 possible filter combinations for a given set of \mathbf{a}_i and \mathbf{b}_i yielding correlation measurements y_1 through y_{16} ;

$$\begin{array}{c} \text{Position} \\ \text{Filters} \end{array} \left\{ \begin{array}{c} \mathcal{T}\mathcal{T} \\ \mathcal{T}\mathcal{R} \\ \mathcal{R}\mathcal{T} \\ \mathcal{R}\mathcal{R} \end{array} \right\} \begin{array}{c} \overbrace{\text{Momentum Filters}} \\ \mathcal{T}\mathcal{T} \quad \mathcal{T}\mathcal{R} \quad \mathcal{R}\mathcal{T} \quad \mathcal{R}\mathcal{R} \\ \left(\begin{array}{cccc} y_1 & y_2 & y_3 & y_4 \\ y_5 & y_6 & y_7 & y_8 \\ y_9 & y_{10} & y_{11} & y_{12} \\ y_{13} & y_{14} & y_{15} & y_{16} \end{array} \right) \sum_{\text{cols}} = \begin{pmatrix} B^{\mathcal{T}\mathcal{T}} \\ B^{\mathcal{T}\mathcal{R}} \\ B^{\mathcal{R}\mathcal{T}} \\ B^{\mathcal{R}\mathcal{R}} \end{pmatrix} \\ \sum_{\text{rows}} = \\ (A^{\mathcal{T}\mathcal{T}} \quad A^{\mathcal{T}\mathcal{R}} \quad A^{\mathcal{R}\mathcal{T}} \quad A^{\mathcal{R}\mathcal{R}}) \end{array} \quad (\text{A12})$$

By summing over rows (position) or columns (momentum), we can separate the position and momentum measurements up to the effect of measurement disturbance, which we have previously established is just a small amount of Gaussian noise—this noise is included in the model via $\mathbf{\Phi}^{(k)}$ and $\mathbf{\Phi}^{(x)}$. By summing outcomes of like-acting filters ($\mathcal{T}\mathcal{T}$ and $\mathcal{R}\mathcal{R}$) and taking the difference of opposing filters ($\mathcal{T}\mathcal{R}$ and $\mathcal{R}\mathcal{T}$), measurement values $Y_i^{(k)}$ and $Y_i^{(x)}$ corresponding to \mathbf{A}_i and \mathbf{B}_i are generated.

$$\begin{aligned} Y_i^{(k)} &= \frac{A_i^{\mathcal{T}\mathcal{T}} - A_i^{\mathcal{R}\mathcal{T}} - A_i^{\mathcal{T}\mathcal{R}} + A_i^{\mathcal{R}\mathcal{R}}}{A_i^{\mathcal{T}\mathcal{T}} + A_i^{\mathcal{R}\mathcal{T}} + A_i^{\mathcal{T}\mathcal{R}} + A_i^{\mathcal{R}\mathcal{R}}} = \mathbf{A}_i \mathbf{K} + \mathbf{\Phi}_i^{(k)} \\ Y_i^{(x)} &= \frac{B_i^{\mathcal{T}\mathcal{T}} - B_i^{\mathcal{R}\mathcal{T}} - B_i^{\mathcal{T}\mathcal{R}} + B_i^{\mathcal{R}\mathcal{R}}}{B_i^{\mathcal{T}\mathcal{T}} + B_i^{\mathcal{R}\mathcal{T}} + B_i^{\mathcal{T}\mathcal{R}} + B_i^{\mathcal{R}\mathcal{R}}} = \mathbf{B}_i \mathbf{X} + \mathbf{\Phi}_i^{(x)} \end{aligned} \quad (\text{A13})$$

The values in the denominator normalize each measurement to the total coincidences, such that each term represent the probability a particular detection event occurs in each of the four possibilities. It also helps compensate for any drift in the the total, joint intensity over the course of the experiment.

This process is repeated M times to build the full measurement vectors $\mathbf{Y}^{(k)}$ and $\mathbf{Y}^{(x)}$.

4. Simulations with Noise

To investigate the accuracy of our technique, we simulated our technique as a function of measurement number M and average detected flux. For the SPDC state, we use the standard double-Gaussian model [37]

$$|\psi\rangle \propto \int dx_1 dx_2 e^{-\frac{(x_1 - x_2)^2}{8\sigma_-^2}} e^{-\frac{(x_1 + x_2)^2}{16\sigma_p^2}} |x_1\rangle |x_2\rangle, \quad (\text{A14})$$

where σ_p is the transverse standard deviation of the pump laser width and

$$\sigma_- = \sqrt{\frac{9L_z\lambda_p}{20\pi}}. \quad (\text{A15})$$

Here, L_z is the length of the nonlinear crystal and λ_p is the wavelength of the pump laser. For the simulation, we chose $L_z = 1$ mm, $\lambda_p = 400$ nm, and $\sigma_p = .85$ mm. The state was sampled above the Nyquist limit with a window including 3 standard deviations of the double Gaussian in both position and momentum. For computational simplicity, we simulated in one dimension

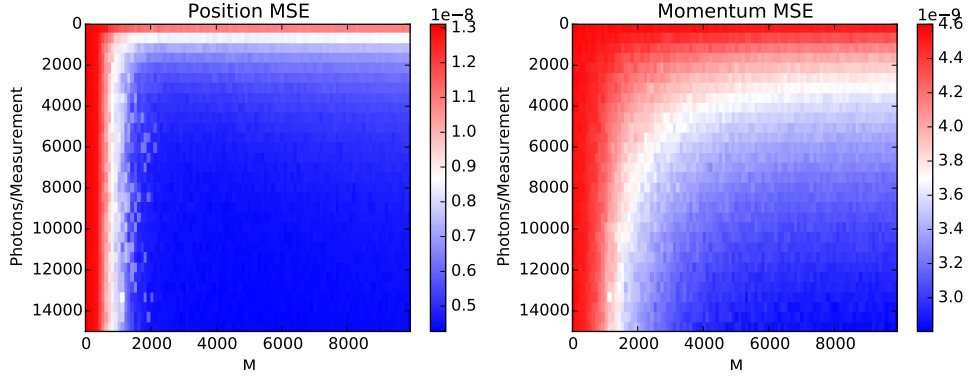


FIG. 7. Simulated MSE in momentum and position as a function of M and average detection events per pattern.

per particle. The state was first filtered in position and then momentum (opposite of the experiment but conceptually identical) by M , 16 pixel local binary filters for a 16×16 dimensional joint state.

The mean-square-error (MSE) of the simulation results with respect to the true distributions is shown in Fig. 7. Compressive sensing reconstruction techniques typically display a sharp phase-shift from poor quality to good quality reconstruction as a function of M and photon flux [57]. This phase change can be clearly seen in the results as the white transition region.

The effect of filtering position introduces extra Gaussian noise into the momentum distribution. This has the effect of shifting the phase transition curve to require slightly higher flux than position—4000 photons/measurement instead of 1000—and to require slightly more measurements, which varies depending on flux. Because total variation minimization (our solver) is effectively a Gaussian denoiser, it removes the noise injected by our filtering so long as we modestly increase flux and measurement number.

5. EPR Steering

EPR Steering is a generalization of the EPR paradox describing non-local correlation stronger than entanglement, but weaker than Bell-nonlocality [50]. Practically, the extent to which a quantum state is steerable is relevant for security in quantum key distribution [53]. The term steering, coined by Schrödinger, refers to the idea that by choosing a measurement basis, Alice can “steer” Bob’s state into an eigenstate of the basis chosen by Alice.

Steering inequalities follow from uncertainty relations—a two-particle quantum state is steerable if its conditional variances in complementary observables are smaller than what the Heisenberg uncertainty relation allows for unconditioned variances. For example, given position and momentum, if $\sigma_{(x_1|x_2)}\sigma_{(k_1|k_2)} < 1/2$, the state is steerable.

Schneeloch *et al.*[58] showed that all classically correlated states satisfy an entropic steering inequality;

$$H(X_1|X_2) + H(K_1|K_2) \geq 2 \log \left(\frac{\pi e}{\Delta_x \Delta_k} \right). \quad (\text{A16})$$

$H(X_1|X_2)$ and $H(K_1|K_2)$ are the discrete, conditional entropies for the binned probability distributions in the position and momentum of particle 1, conditioned on measurements of particle 2. Δ_x and Δ_k refer to the respective position or momentum discretization widths, and the factor of 2 in front of the logarithm on the right-hand side accounts for the transverse position and momentum each having two dimensions. Conceptually, Eq. (A16) states that *strong correlations in measurements of complementary observables is a signature of entanglement*—essentially a restatement of the EPR paradox. Note that the conditional entropies are calculated directly from the measured probability distributions, and not from an inferred quantum state. Despite the fact that the measured distributions are discrete, Eq. (A16) witnesses *continuous-variable* steering.